

## Supplementary Information:

Autocharacterization: Automated and Scalable Semiconductor Property Estimation from High-throughput Experiments using Computer Vision

Alexander E. Siemann<sup>1\*†</sup>, Eunice Aissi<sup>1\*†</sup>, Fang Sheng<sup>1</sup>, Armi Tiihonen<sup>1,2</sup>, Hamide Kavak<sup>1,3</sup>, Basita Das<sup>1</sup>, Tonio Buonassisi<sup>1</sup>

<sup>1</sup>Department of Mechanical Engineering, Massachusetts Institute of Technology, Cambridge, MA 02139, USA

<sup>2</sup>Department of Applied Physics, Aalto University, Espoo, 02150, Finland

<sup>3</sup>Department of Physics, Cukurova University, Adana, 01330, Turkiye

\*Corresponding authors: {asiemann@mit.edu, eunicea@mit.edu}

†Contributed equally.

## Experiments

### Processing Times

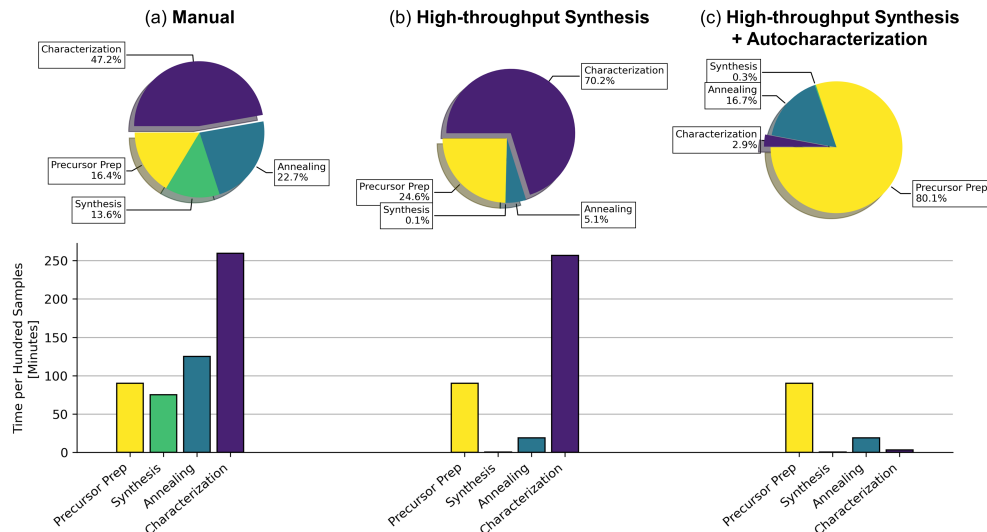


**Fig. S-1:** Minimum time to process 100 perovskite samples and compute band gap. The processing times are shown for three different scenarios: (a) manual synthesis manual and characterization, (b) high-throughput synthesis and manual characterization, and (c) high-throughput synthesis and high-throughput autocharacterization.

In this paper, we aim to achieve higher rate-matching between the synthesis and characterization of materials for high-throughput screening. In Figure S-1, the minimum processing time required to go from precursor to data is illustrated for perovskite samples. The minimum processing times to collect band gap data for 100

perovskite samples are shown and represent the times experimentally recorded during this study. Three different scenarios are represented that use combinations of both manual and high-throughput methods. The processing time to collect these band gap data is further broken down into four steps: (1) precursor preparation, (2) synthesis, (3) annealing, and (4) characterization. These are the *minimum* processing times as they do not account for sample transfer times or reloading, *e.g.*, moving a sample to the hotplate. In Figure S-1b, moving from manual to high-throughput synthesis results in a higher discrepancy of throughputs between synthesis and characterization, which bottlenecks the materials screening loop. However, in Figure S-1c, by using high-throughput autocharacterization, the rate of high-throughput synthesis is closely matched to that of high-throughput synthesis, in turn, enabling more efficient materials screening. The bottleneck then becomes precursor preparation, which is out of the scope of this study.

To detail the individual processing time contributions in this study, precursor preparation is always conducted manually and takes 90 minutes to make 100 samples worth of solution for all three scenarios. Synthesis takes 45 seconds per sample for manual spin coating and takes 20 seconds per 100 samples for high-throughput manufacturing. Annealing takes 10 minutes for manual thin films where 8 samples can fit on a single hot plate at a time. It takes 15 minutes for the thicker, high-throughput samples but all 100 samples can fit on a single hot plate. Characterization for computing band gap takes 255 minutes per 100 samples manually by a domain expert. It takes 3 minutes per 100 samples using the band gap extractor autocharacterization algorithm developed in this paper.

### Experimental Reproducibility

Variability exists across samples manufactured using our high-throughput combinatorial printer, as the setup is designed for low-cost, scalable, and high-throughput screening rather than high-fidelity experiments. Although the purpose of the paper is not to highlight the perovskite manufacturing method but to focus on the rate matching of characterization, it is important to understand the sources of variability from experiment to experiment, as these sources of variability will arise for those who replicate the proposed approaches. Figure S-2 shows the post-degradation structural morphology differences between two of the same sample compositions across two separate batches, manufactured using the same printing conditions. Both batches were degraded under the same environmental conditions for 2 hours at 35°C, 40% relative humidity, and 0.5 suns of AM1.5 illumination (without UV). During crystallization, batch A achieved more uniform and compact grain boundaries, whereas the crystallization in sample B produced jagged boundaries, inducing more pathways for degradation. This crystallization mismatch explains the accelerated degradation noted in batch B relative to batch A. Samples that are prone to phase changes (*e.g.*, compositions near phase boundaries such as  $0.0 \leq x \leq 0.15$ , for  $\text{FA}_{1-x}\text{MA}_x\text{PbI}_3$ ), may experience high sample-to-sample variances using any sample preparation approach. Therefore, the effects of these variations must be carefully considered in high-throughput manufacturing scenarios, where not every sample can be fully characterized at high fidelity. These morphological variations in the high-throughput manufacturing process must be further studied to ascertain better control over experimental reproducibility. In this

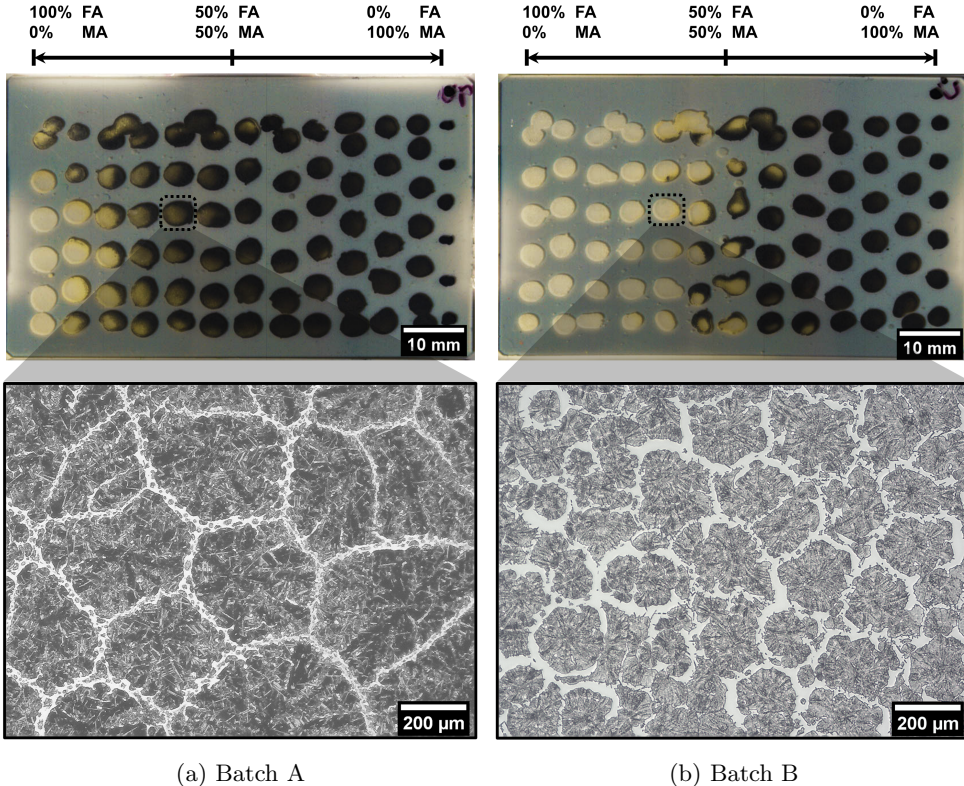


**Fig. S-2:** Optical microscopy of deposit morphology between two different batches of  $\text{FA}_{0.67}\text{MA}_{0.33}\text{PbI}_3$  after controlled degradation.

study, three batches of samples were selected with similar morphology in an attempt to minimize this variation and maintain the emphasis of the paper on the assessment of the proposed automatic characterization methods, rather than on the method of synthesis.

## Material Characterization

### Computer Vision Segmentation and Composition Mapping

Figures S-4a-b illustrate the process of going from a raw hyperspectral datacube ( $\Omega$ ) to computer vision-segmented data ( $\Phi$ ), which is used as input to the autocharacterization methods developed in this paper. An image,  $\Omega$ , which can be in either Hyperspectral or RGB format, is segmented using Algorithm 1, producing the segmented pixels,  $(\hat{X}, \hat{Y})$ , and their corresponding set of reflectance values,  $R(\lambda)$ . The matched sets of  $(\hat{X}, \hat{Y})$  and  $R(\lambda)$  are denoted as  $\Phi$ . The compositions of each deposited sample are then able to be mapped onto the segmented  $\Phi$  using the G-code raster path of the printer head, the pump speed traces from Figure S-3, and Equation 1.

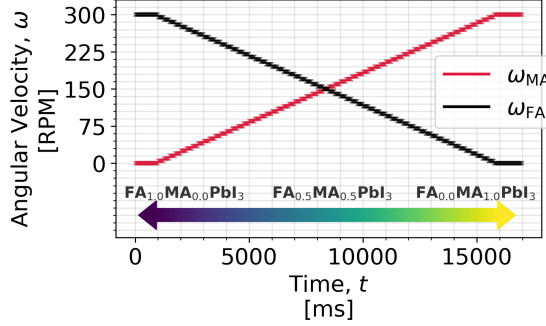


**Fig. S-3:** Traces of motor velocity over time for each perovskite precursor,  $\text{MAPbI}_3$  and  $\text{FAPbI}_3$ , for high-throughput combinatorial deposition as droplets.

Figure S-4c illustrates this complete mapping of all material deposits with their derived compositions within the  $\text{FA}_{1-x}\text{MA}_x\text{PbI}_3$  series.

### Band Gap

The materials within the  $\text{FA}_{1-x}\text{MA}_x\text{PbI}_3$  compositional series are direct band gap semiconductors [67, 68]. To compute the band gap of these materials, first, the reflectance spectra of all samples are measured using a hyperspectral camera (Resonon Pika L) that measures reflectance within the wavelength range  $\lambda \in [380\text{nm}, 1020\text{nm}]$  at 2nm resolution. Figure S-5 illustrates the measured reflectance spectra for all  $N = 201$  samples in the paper, gathered using the computer vision-segmentation of the raw hyperspectral datacube, as shown in Figure S-4. Then, the reflectance spectra are converted to their corresponding absorption spectra using the Kubelka-Munk equation [19, 55] for sufficiently thick samples (the thickness of our samples is approximately  $300\mu\text{m}$  – which is considered sufficiently thick for reflectance measurement):

$$F(R) = \frac{(1 - R)^2}{2R}, \quad (\text{S-2})$$

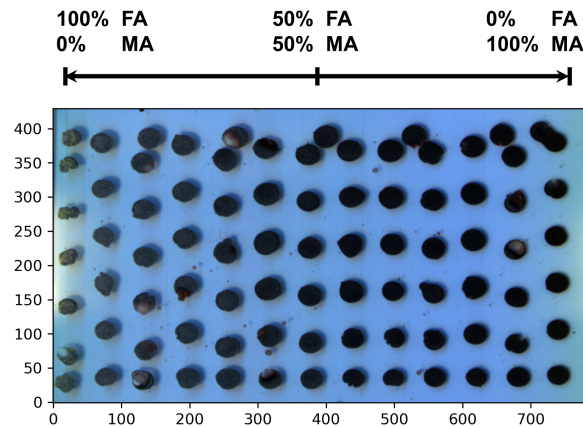
where  $R$  is the reflectance for the entire range of  $\lambda$  for a given segmented pixel in the reflectance hypercube,  $(\hat{X}, \hat{Y})$ . Next, the Tauc curves are computed from  $F(R)$  [54]:

$$(F(R) \cdot h\nu)^{1/\gamma} = B(h\nu - E_g), \quad (\text{S-3})$$

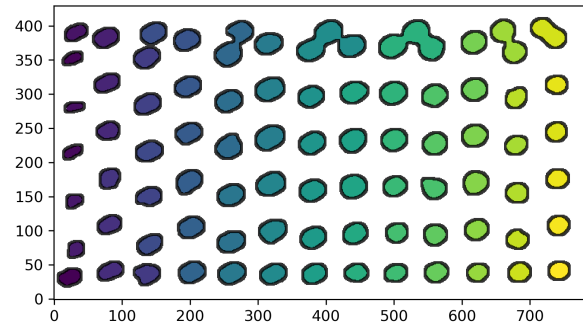
where  $h\nu$  is energy ( $h\nu = \frac{1240}{\lambda}$ ),  $\gamma = \frac{1}{2}$  for direct band gap and  $\gamma = 2$  for indirect band gap,  $B$  is a constant that allows the band gap,  $E_g$ , to be the x-intercept of a regression fit line to the slope of Tauc curve. Hence, the following equation arises that enables computation of the direct band gap from the initial reflectance spectra by equating Equation S-4 to Equation S-3:

$$(F(R) \cdot h\nu)^2 = \left( \frac{(1 - R)^2}{2R} \cdot \frac{1240}{\lambda} \right)^2 = \left( \frac{620(1 - R)^2}{\lambda R} \right)^2. \quad (\text{S-4})$$

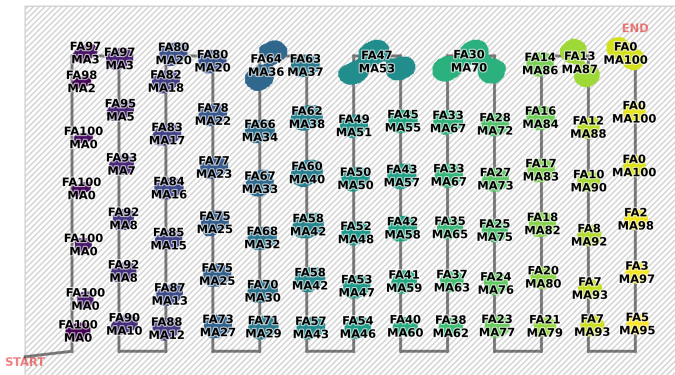
In this paper, we use the theory formulated above from optics to automatically compute the median band gap across all vision-segmented pixels  $(\hat{X}, \hat{Y})$  for a given



(a) Raw Image



(b) Computer Vision-segmented Image



### (c) Automated Composition Extraction Overlay

**Fig. S-4:** Computer vision segmentation and composition mapping.

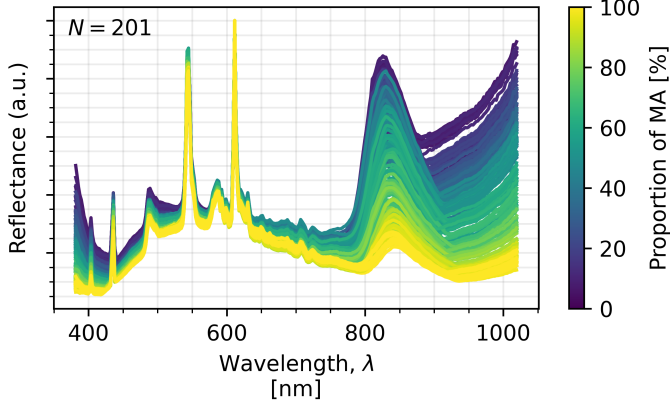


**Fig. S-5:** Hyperspectral reflectance of all  $N = 201$  samples synthesized in this study, color mapped as a function of composition.

perovskite sample, as described by the autocharacterization algorithm illustrated in Figure 4. Currently, the autocharacterization algorithm is configured to operate only on materials with a single direct band gap. The band gaps computed using the automatic Tauc segmentation and regression RMSE minimization processes employed by the autocharacterization algorithms are benchmarked against the band gaps calculated manually by a domain expert. This band gap comparison between algorithm and expert is used to determine an accuracy metric for the algorithm, assuming the expert-calculated output as ground truth. The accuracy is calculated by taking the average of a binary 0/1 for all  $N = 201$  samples, determined based on whether or not the differences between the automatic and the expert band gap values fall within a specified energy difference threshold (shown along the  $x$ -axis of Figure S-6b).

Figure S-6a illustrates the autocharacterization output band gaps as a function of composition for the three independent batches. Figure S-6b illustrates the accuracy of the automatic algorithm as a function of the energy difference threshold. The algorithm achieves 98.5% accuracy within 0.02eV and as the threshold becomes tighter, the algorithm accuracy is expected to decrease.

### Stability

To conduct the degradation experiments in this paper, we put the samples in a degradation chamber and monitor the conditions for 2 hours, capturing RGB images (Thorlabs DCC1645C camera with the infrared filter removed to increase sensitivity towards dark samples) every 30 seconds. The construction and operation of the degradation chamber setup are detailed in Keesey & Tiihonen *et al.* [8]. Figure S-7(a) shows the time series of temperature and humidity conditions over the course of the experiment. Over the 2-hour degradation experiment, the temperature conditions were maintained at  $34.5^{\circ}\text{C} \pm 0.5^{\circ}\text{C}$  with a relative humidity of  $40\% \pm 1\%$ . An initial jump in temperature with a respective dip in humidity is noted as the samples are placed into the degradation chamber before the internal environment equilibrates. A

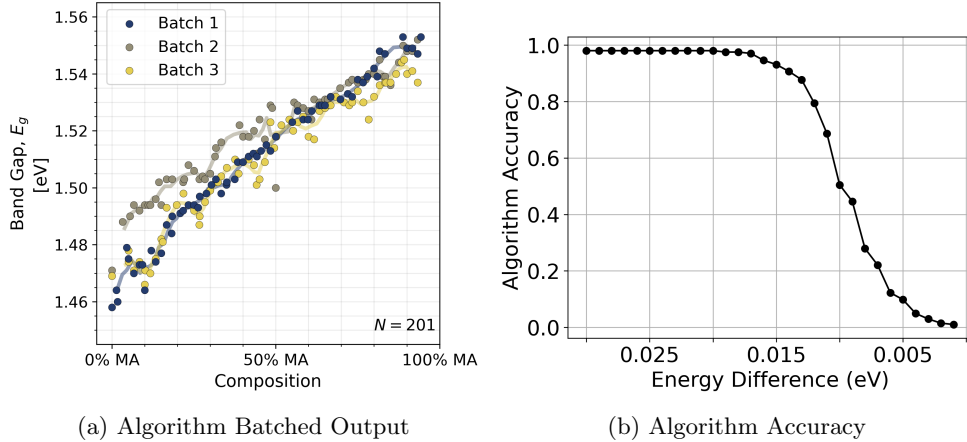


**Fig. S-6:** (a) Direct band gap values output by the automatic band gap extraction algorithm, split by batch, as a function of  $FA_{1-x}MA_xPbI_3$  composition. (b) Automatic band gap extraction algorithm accuracy as a function of the maximum allowable difference in energy between the domain expert-calculated and automatically calculated band gaps.

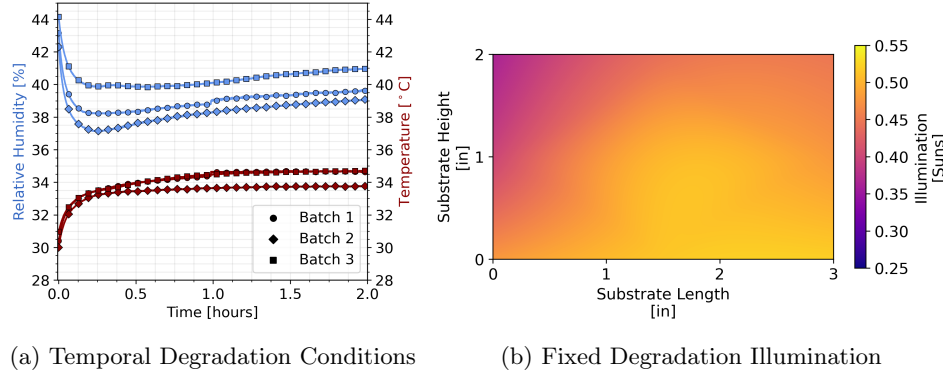


**Fig. S-7:** (a) Temporal degradation conditions for each of the 3 batches of samples over the course of 2 hours, measured using a temperature and humidity sensor (Adafruit, AHT10). (b) Spatial uniformity of illumination measured across the substrate within the degradation chamber, measured using a lux sensor (Adafruit, VEML7700).

class AAA solar simulator (G2V Optics Sunbrick Base, with visible-only part of the AM1.5G spectrum) is used to illuminate the  $3'' \times 2''$  substrate of samples during the 2-hour degradation experiment. Figure S-7(b) shows the spatial uniformity of the illumination across the substrate internal to the degradation chamber, measured using a lux sensor (Adafruit, VEML7700). These illumination conditions are held fixed over

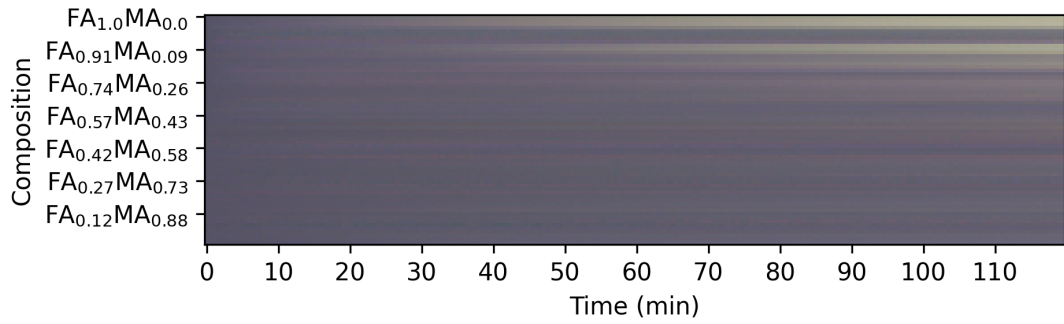
the course of the experiment. Most of the substrate experiences 0.50-0.55 suns of illumination, however, in the top-left corner of the substrate, a dip in illumination occurs as a result of minor occlusion due to sensor placement. Figure S-8 illustrates that this dip in illumination at the top-left corner of the substrate does not have a major effect on the degradation pattern of the  $FA_{1-x}MA_xPbI_3$  compositional series. Degradation, as indicated by the yellowing, is shown to begin in the formamidinium (FA)-rich end of the samples and migrates towards the methylammonium (MA)-rich end over time.



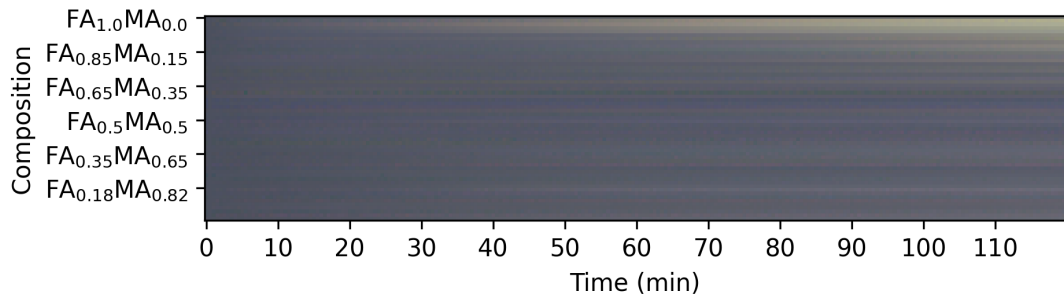
**Fig. S-8:** Degradation of the high-throughput manufactured  $FA_{1-x}MA_xPbI_3$  compositional series over 2 hours.

After segmenting each sample across the entire time domain of the experiment, the full matrix of degradation time series is populated and color calibrated automatically, as shown in Figure S-9. In this specific experiment, spatial non-uniformity of reflected surfaces was detected in the post-analysis, which does not noticeably affect the instability index calculation but does give rise to artificial color differences in the samples, depending on their location on the substrate. These spatially-dependent color differences arise due to the physical configuration of the environmental chamber and the RGB camera. To account for these color differences in the final output matrix time series, an additional color correction step was applied that initializes all deposited samples to the same color. This color correction is only cosmetic and was not used in the calculations for determining the degradation intensity,  $I_c$ . Color correction aids in the interpretation of the visualized time series data by making the color changes due to degradation easier to see while diminishing the unwanted effects of spatially-dependent reflectivity aberrations. After the color correction, a fully calibrated matrix of degradation time-series is acquired, showing the color change over time for each perovskite sample within its batch, shown in Figure S-9.

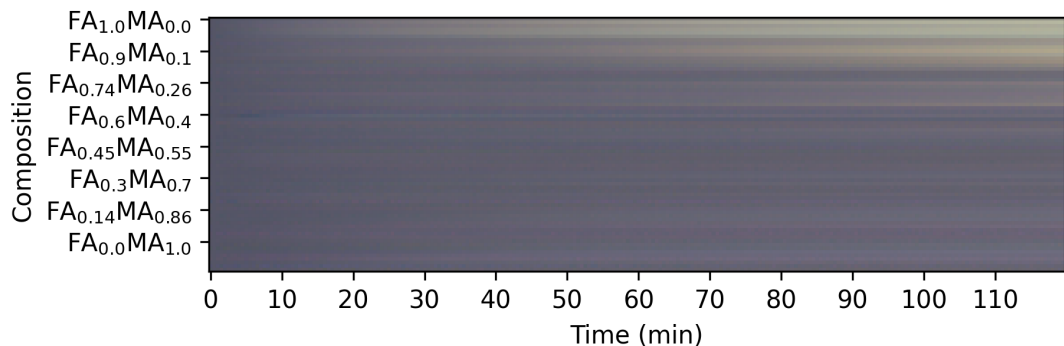
The degradation intensity,  $I_c$ , is computed from the color-changing time series per sample using Equation 3 [7, 8]. The degradation detection algorithm automatically computes  $I_c$  for every sample. High values of  $I_c$  correspond to high degradation. To benchmark the algorithm, the difference in domain expert-computed band gaps before and after degradation is used as a ground truth to quantify whether the material has truly degraded or not. This is possible due to the change in band gap that occurs in perovskites during either a phase transition or chemical decomposition [7, 63]. Hence, in Figure S-10(a), any expert-calculated post-degraded band gaps (red points) samples that fall outside of the  $\pm 0.02\text{eV}$  bounds, with respect to the regression fit line to the expert-calculated pre-degradation band gaps (blue points), are considered to exhibit “Ground Truth Degradation”. These ground truth-degraded samples are denoted by yellow scatter points in Figure S-10(b). The bounds of  $\pm 0.02\text{eV}$  are used because they empirically fit the expert-calculated pre-degradation band gaps (blue points) with



(a) Stability Time Series for Batch 1



(b) Stability Time Series for Batch 2



(c) Stability Time Series for Batch 3

**Fig. S-9:** Final stability time series matrix of all batches of segmented droplets over the course of a 2-hour degradation experiment. All samples begin the experiment colored as dark gray and over the course of degradation, samples with MA proportions between 0% to 20% exhibit yellowing around the 20min to 40min mark, thus indicating degradation.

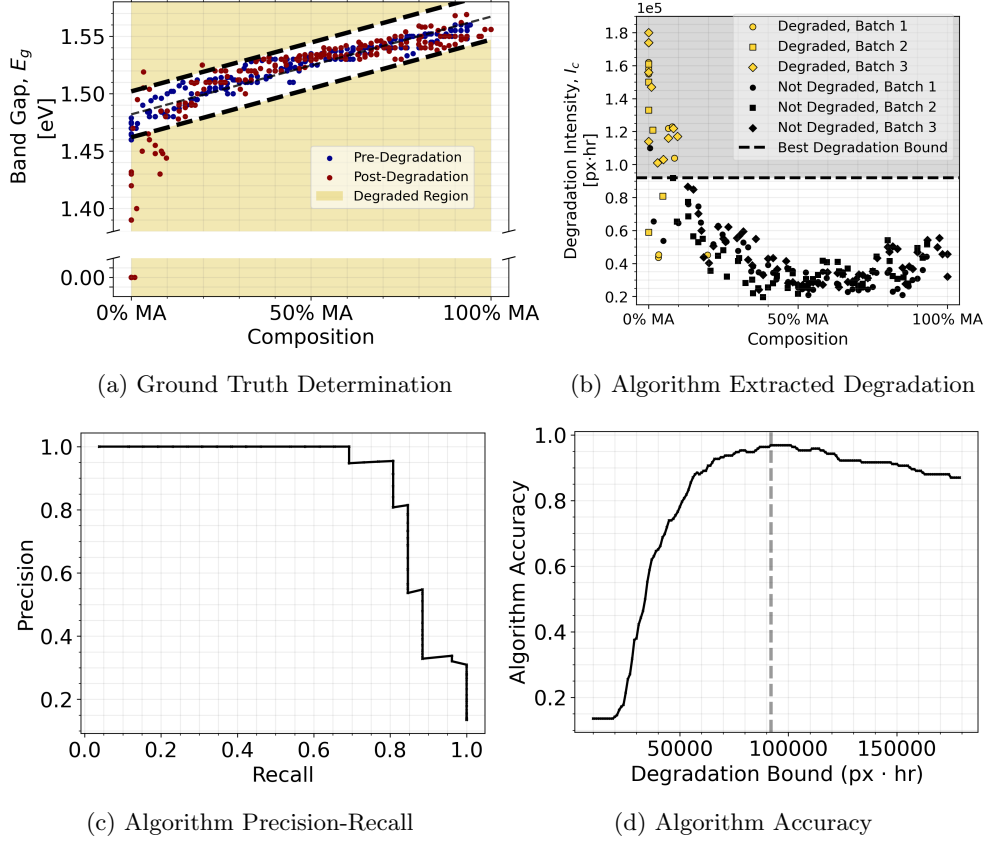


**Fig. S-10:** Automatic degradation detection algorithm performance benchmarking. (a) Shows how the ground truth degradation is determined using post-degradation band gap measurement. The break in the graph is used to visualize which compositions had no band gap after degradation, reported as 0.0eV. (b) Values of  $I_c$  as a function of composition, split by batch with a total of  $N = 201$  samples.  $I_c$  is used as a classifier for degradation, where the dashed line indicates the separation of high  $I_c$  versus low  $I_c$ . (c) Precision-recall performance of  $I_c$  as a classifier for degradation based on the classification rate of false negatives and false positives. (d) Accuracy of  $I_c$  as a classifier for determining high and low degradation. The  $x$ -axis indicates the decision boundary value of  $I_c$ , where values above are considered degraded and values below are not. The optimal value of  $I_c$  as a decision boundary for degradation is  $I_c = 0.92 \times 10^5$  px·hr, and is shown as a dashed vertical line. This value is where the accuracy of the algorithm is maximum at 96.9%.

little to no tolerance. Thus, the region where “Ground Truth Degradation” occurs in the post-degraded samples is indicated by the yellow shaded region in Figure S-10(a).

Figure S-10(b) illustrates that the magnitude of  $I_c$  strongly corresponds with the ground truth determination of degradation using band gap difference as a metric. This correspondence can be quantified using the precision-recall (PR) of the autocharacterization algorithm. A PR curve quantifies the performance of using a classifier, in this case,  $I_c$ , to predict a ground truth, in this case, degradation:

$$\text{Recall} = \frac{TP}{TP + FN}$$

$$\text{Precision} = \frac{TP}{TP + FP}, \quad (\text{S-5})$$

where  $TP$  are the true positives,  $FN$  are the false negatives,  $FP$  are the false positives. We use the PR curve instead of the ROC (receiver operating characteristic) curve here due to the large class imbalance between the number of degraded samples versus non-degraded samples (there are significantly more non-degraded samples than there are degraded samples).

Figure S-10(c) illustrates the PR curve of the automatic degradation detection algorithm based on the degradation decision boundary (horizontal black dashed line in Figure S-10b). The goal is to have both high precision and high recall simultaneously. The PR-AUC (precision-recall area under the curve) figure of merit boils the PR curve down to a single number that determines the performance of  $I_c$  as a good predictor for degradation. The value of PR-AUC falls between 0.0 and 1.0, where a value of 1.0 represents perfect performance. The  $I_c$  values computed by the autocharacterization algorithm achieve a PR-AUC of  $0.853 \in [0, 1]$ , implying that high values of  $I_c$  do strongly correspond to ground truth degradation. Figure S-10d shows the effect of moving the decision boundary on the accuracy in detecting the degradation. Considering recall, precision, and accuracy,  $I_c$  performs optimally, with an accuracy of 96.9%, in detecting degraded samples when the decision boundary is set to  $0.92 \times 10^5 \text{px}\cdot\text{hr}$ . However, accuracies of over 90% are achieved for a wide range of  $I_c$  decision boundaries:  $0.7 \times 10^5 \text{px}\cdot\text{hr} \leq I_c \leq 1.6 \times 10^5 \text{px}\cdot\text{hr}$ . Hence, indicating that  $I_c$  is a general yet strong predictor of degradation.

### Phase and Elemental Analysis

Phase analysis, such as X-ray diffraction (XRD), of perovskites is used to determine the structure and quality of the manufactured samples. In this study, we measure our samples using the Bruker X-ray Diffractometer with a Cobalt Source D8 and General Area Detector Diffraction System. Figure S-11 illustrates the pre- and post-degradation XRD traces for equally spaced compositions along the  $\text{FA}_{1-x}\text{MA}_x\text{PbI}_3$  series. The reference peak locations for both the favorable cubic  $\alpha$ -FAPbI<sub>3</sub> [61] and favorable tetragonal MAPbI<sub>3</sub> phases [62] are shown together as black vertical lines and “\*” symbols since a shift of only  $\Delta 2\theta \approx 0.16^\circ$  is seen from FAPbI<sub>3</sub> to MAPbI<sub>3</sub> at around the  $2\theta = 31.5^\circ$  peak. High-resolution scans of this peak shift along  $\text{FA}_{1-x}\text{MA}_x\text{PbI}_3$  are shown in Figure 3b and can be used as an additional validation tool for composition shift. During degradation, FAPbI<sub>3</sub> phase transitions from a favorable cubic  $\alpha$ -phase to a non-perovskite hexagonal  $\delta$ -phase [61]. Hence, XRD is a

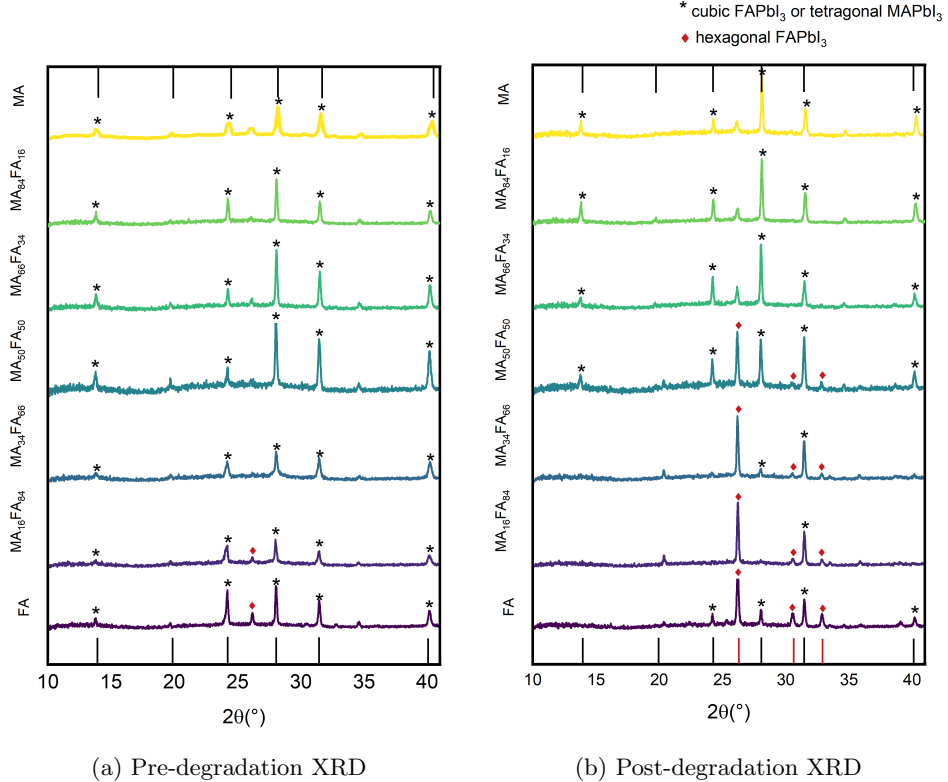


**Fig. S-11:** XRD peak intensities for uniformly-spaced compositions along the  $\text{FA}_{1-x}\text{MA}_x\text{PbI}_3$  series before and after degradation.

useful validation tool for pre- and post-degradation determination. Prior to degradation, Figure S-11a illustrates that the samples exhibit high adherence to their favorable phases with only minor contribution of  $\delta$ - $\text{FAPbI}_3$  phase. However, after the degradation test, Figure S-11b illustrates high degradation (indicated by the high peak intensities of the  $\delta$ - $\text{FAPbI}_3$  phase at  $2\theta = 26.3^\circ$ , denoted by the red diamond) in the FA-rich compositions. This XRD result matches the detected yellowing degradation pattern of the FA-rich samples, as shown in Figure S-8 and Figure S-9.

Elemental analysis, such as X-ray photoelectron spectroscopy (XPS), is used to determine the shift in the binding energy of bonds present within the different A-site cations (FA and MA) along the  $\text{FA}_{1-x}\text{MA}_x\text{PbI}_3$  series, in turn corresponding to a “composition” shift. XPS is a surface-sensitive quantitative spectroscopic technique that can identify crystalline phases. In this study, we measure our samples using the PHI 5000 Versa Probe II Focus X-ray Photoelectron Spectrometer, equipped with a monochromated  $\text{AlK}\alpha$  X-ray source for excitation at 1486.6eV with an X-ray beam size of  $200\mu\text{m}$ . Survey spectra of  $\text{FAPbI}_3$  to  $\text{MAPbI}_3$  series are depicted in Figure S-12. Using the survey spectra alone, there are variations in A-site composition that can

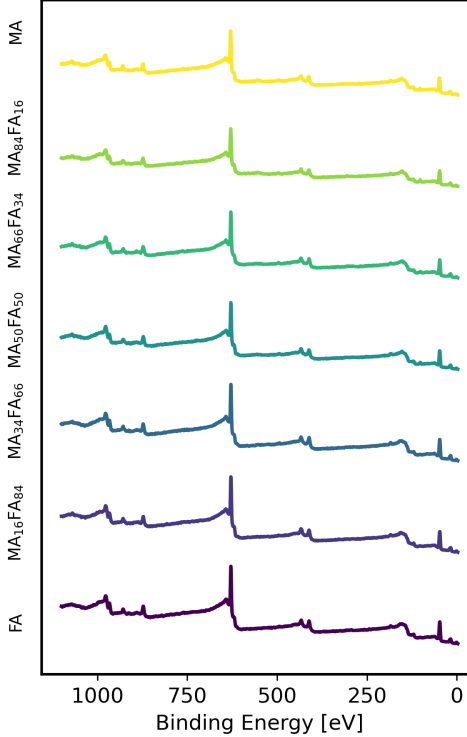


**Fig. S-12:** Full XPS spectra for uniformly-spaced compositions along the  $\text{FA}_{1-x}\text{MA}_x\text{PbI}_3$  series.

not be distinguished clearly in survey spectra due to the many similarities between the FA and MA molecules [50]. However, the primary distinguishing feature of these is the presence of the carbon-nitrogen double bond (C=N), clearly detectable in the high-resolution XPS scans, as shown in Figure 3c. In the high-resolution scans of C1s1 and N1s2, the calibration is performed on the lowest C1s energy peak of 284.8eV. Hence, the shift in C=N peak intensity quantifies the presence of FA relative to MA, in turn, determining composition along the  $\text{FA}_{1-x}\text{MA}_x\text{PbI}_3$  series.

Figure S-13 shows the quantitative XRD peak shifts and XPS peak intensities from the high-resolution scans for the phase and elemental shifts that occur along the  $\text{FA}_{1-x}\text{MA}_x\text{PbI}_3$  series. The XRD peak of the (012) crystallographic plane shifts from lower to higher  $2\theta$  angles as more MA is added to the composition. Conversely, the XPS peak for the presence of C=N bonds shifts from higher to lower intensity as more MA is added to the composition. Thus, both of these measurements validate the presence of a compositional gradient occurring across the synthesized batches of samples.

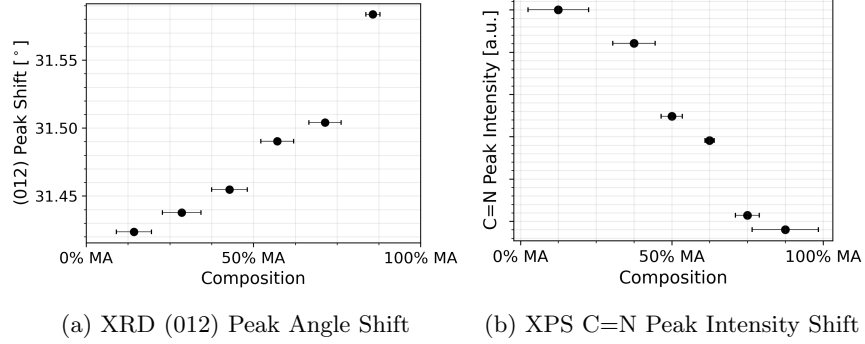


**Fig. S-13:** (a) XRD 2 $\theta$  values for the (012) crystallographic plane peak shift from FA-rich to MA-rich  $\text{FA}_{1-x}\text{MA}_x\text{PbI}_3$  compositions. (b) XPS intensity shift for the C=N peak from FA-rich to MA-rich  $\text{FA}_{1-x}\text{MA}_x\text{PbI}_3$  compositions. The horizontal error bars illustrate the relative widths of the XRD and XPS peaks.

### Size of the Perovskite Search Space

A commonly explored metal halide perovskite search space for photovoltaic applications from literature consists of the following eight-component material system:  $(\text{FA}_x\text{MA}_y\text{Cs}_{1-x-y})(\text{Pb}_z\text{Sn}_{1-z})(\text{Br}_a\text{Cl}_b\text{I}_{1-a-b})_3$  [7, 9, 14, 22–24]. Figure S-14 shows the discretization of these eight components within the archetypal  $\text{ABX}_3$  perovskite structure. The number of steps per edge,  $n$ , determines the compositional resolution for each subspace. As the number of steps increases, the number of potential compositions increases, and, in turn, the search space becomes more vast. For this eight-component search space, the number of possible compositions is proportional to the product of each subspace's (A, B, and X) step size to the power of the number of components within each subspace (here, 3-components for A (FA, MA, and Cs), 2-components for B (Pb and Sn), and 3-components for X (Br, Cl, and I))  $\Rightarrow n^3 \times n \times n^3$  for the  $\text{A} \times \text{B} \times \text{X}$  subspaces. A caveat in this equation is that for binary subspaces, the power of the step size is 1 instead of 2 since the space is linear, as shown by the B-site subspace in Figure S-14. Hence, for a low-resolution search space of  $n = 10$  steps,  $1 \times 10^6$  total compositions are considered; and for a high-resolution search space of  $n = 100$  steps,  $7 \times 10^{12}$  compositions are considered.

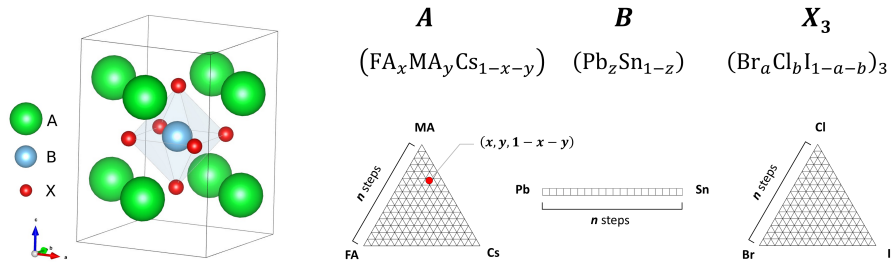


**Fig. S-14:** Archetypal metal halide perovskite compositional search space.

## Full Experimental Results

Table S-1 contains the full readout of the characterization results extracted by the autocharacterization algorithms for all  $N = 201$  samples. We report the numerical values of calculated composition, autocharacterization-calculated band gap (Auto  $E_g$ ), human domain expert-calculated band gap (Expert  $E_g$ ), autocharacterization-calculated degree of degradation ( $I_c$ ), and the ground truth degradation determined by the human domain expert. Dashes indicate values unable to be determined for that composition due to missing data.

**Table S-1:** Results readout for all perovskite samples produced in this study.

Sample	Computed Composition	Auto $E_g$ (eV)	Expert $E_g$ (eV)	$I_c$ (px·hr) $\times 10^5$	Degradation (Ground Truth)
1	FA <sub>1.000</sub> MA <sub>0.000</sub> PbI <sub>3</sub>	1.471	1.460	1.581	Yes
2	FA <sub>1.000</sub> MA <sub>0.000</sub> PbI <sub>3</sub>	1.463	1.474	1.737	Yes
3	FA <sub>1.000</sub> MA <sub>0.000</sub> PbI <sub>3</sub>	1.463	1.475	1.562	Yes
4	FA <sub>1.000</sub> MA <sub>0.000</sub> PbI <sub>3</sub>	1.467	1.479	1.799	Yes
5	FA <sub>1.000</sub> MA <sub>0.000</sub> PbI <sub>3</sub>	1.458	1.464	1.335	Yes
6	FA <sub>1.000</sub> MA <sub>0.000</sub> PbI <sub>3</sub>	1.469	1.470	1.739	Yes
7	FA <sub>1.000</sub> MA <sub>0.000</sub> PbI <sub>3</sub>	1.454	1.460	1.465	Yes
8	FA <sub>1.000</sub> MA <sub>0.000</sub> PbI <sub>3</sub>	1.455	1.470	-	Yes
9	FA <sub>1.000</sub> MA <sub>0.000</sub> PbI <sub>3</sub>	1.450	1.460	-	Yes
10	FA <sub>1.000</sub> MA <sub>0.000</sub> PbI <sub>3</sub>	1.457	1.470	-	Yes
11	FA <sub>1.000</sub> MA <sub>0.000</sub> PbI <sub>3</sub>	1.457	1.465	1.607	Yes
12	FA <sub>1.000</sub> MA <sub>0.000</sub> PbI <sub>3</sub>	1.475	1.475	1.501	No
13	FA <sub>1.000</sub> MA <sub>0.000</sub> PbI <sub>3</sub>	1.473	1.470	1.098	Yes
14	FA <sub>1.000</sub> MA <sub>0.000</sub> PbI <sub>3</sub>	1.471	1.470	1.623	Yes
15	FA <sub>0.987</sub> MA <sub>0.013</sub> PbI <sub>3</sub>	1.464	1.470	1.209	Yes
16	FA <sub>0.983</sub> MA <sub>0.017</sub> PbI <sub>3</sub>	1.460	1.474	0.655	No
17	FA <sub>0.968</sub> MA <sub>0.032</sub> PbI <sub>3</sub>	1.488	1.490	0.436	Yes
18	FA <sub>0.955</sub> MA <sub>0.045</sub> PbI <sub>3</sub>	1.479	1.484	0.453	Yes
19	FA <sub>0.950</sub> MA <sub>0.050</sub> PbI <sub>3</sub>	1.474	1.480	0.809	Yes
20	FA <sub>0.950</sub> MA <sub>0.050</sub> PbI <sub>3</sub>	1.475	1.484	0.538	No
21	FA <sub>0.950</sub> MA <sub>0.050</sub> PbI <sub>3</sub>	1.478	1.485	1.012	Yes
22	FA <sub>0.945</sub> MA <sub>0.055</sub> PbI <sub>3</sub>	1.490	1.494	1.034	Yes
23	FA <sub>0.933</sub> MA <sub>0.067</sub> PbI <sub>3</sub>	1.471	1.480	1.215	Yes
24	FA <sub>0.933</sub> MA <sub>0.067</sub> PbI <sub>3</sub>	1.470	1.480	1.165	Yes
25	FA <sub>0.933</sub> MA <sub>0.067</sub> PbI <sub>3</sub>	1.494	1.497	1.223	Yes
26	FA <sub>0.917</sub> MA <sub>0.083</sub> PbI <sub>3</sub>	1.473	1.484	1.040	Yes
27	FA <sub>0.917</sub> MA <sub>0.083</sub> PbI <sub>3</sub>	1.474	1.485	0.918	No
28	FA <sub>0.917</sub> MA <sub>0.083</sub> PbI <sub>3</sub>	1.492	1.496	1.231	Yes
29	FA <sub>0.907</sub> MA <sub>0.093</sub> PbI <sub>3</sub>	1.473	1.482	0.652	No
30	FA <sub>0.900</sub> MA <sub>0.100</sub> PbI <sub>3</sub>	1.464	1.480	1.170	Yes
31	FA <sub>0.900</sub> MA <sub>0.100</sub> PbI <sub>3</sub>	1.466	1.485	-	-

**Table S-1:** Continued from previous page.

Sample	Computed Composition	Auto $E_g$ (eV)	Expert $E_g$ (eV)	$I_c$ (px·hr)×10 <sup>5</sup>	Degradation (Ground Truth)
32	FA <sub>0.900</sub> MA <sub>0.100</sub> PbI <sub>3</sub>	1.494	1.500	0.645	No
33	FA <sub>0.898</sub> MA <sub>0.102</sub> PbI <sub>3</sub>	1.471	1.480	-	-
34	FA <sub>0.889</sub> MA <sub>0.111</sub> PbI <sub>3</sub>	1.494	1.502	-	-
35	FA <sub>0.883</sub> MA <sub>0.117</sub> PbI <sub>3</sub>	1.470	1.480	-	-
36	FA <sub>0.883</sub> MA <sub>0.117</sub> PbI <sub>3</sub>	1.494	1.502	-	-
37	FA <sub>0.881</sub> MA <sub>0.119</sub> PbI <sub>3</sub>	1.478	1.487	-	No
38	FA <sub>0.867</sub> MA <sub>0.133</sub> PbI <sub>3</sub>	1.496	1.507	0.759	No
39	FA <sub>0.867</sub> MA <sub>0.133</sub> PbI <sub>3</sub>	1.474	1.490	0.773	No
40	FA <sub>0.867</sub> MA <sub>0.133</sub> PbI <sub>3</sub>	1.475	1.487	0.684	No
41	FA <sub>0.857</sub> MA <sub>0.143</sub> PbI <sub>3</sub>	1.502	1.510	0.866	-
42	FA <sub>0.850</sub> MA <sub>0.150</sub> PbI <sub>3</sub>	1.494	1.505	0.851	No
43	FA <sub>0.850</sub> MA <sub>0.150</sub> PbI <sub>3</sub>	1.477	1.490	0.565	No
44	FA <sub>0.850</sub> MA <sub>0.150</sub> PbI <sub>3</sub>	1.482	1.490	0.849	No
45	FA <sub>0.846</sub> MA <sub>0.154</sub> PbI <sub>3</sub>	1.481	1.490	0.438	No
46	FA <sub>0.833</sub> MA <sub>0.167</sub> PbI <sub>3</sub>	1.487	1.495	0.529	No
47	FA <sub>0.833</sub> MA <sub>0.167</sub> PbI <sub>3</sub>	1.493	1.500	0.703	No
48	FA <sub>0.833</sub> MA <sub>0.167</sub> PbI <sub>3</sub>	1.503	1.510	0.747	No
49	FA <sub>0.819</sub> MA <sub>0.181</sub> PbI <sub>3</sub>	1.484	1.495	0.649	No
50	FA <sub>0.817</sub> MA <sub>0.183</sub> PbI <sub>3</sub>	1.503	1.512	0.549	No
51	FA <sub>0.817</sub> MA <sub>0.183</sub> PbI <sub>3</sub>	1.490	1.495	0.600	No
52	FA <sub>0.803</sub> MA <sub>0.197</sub> PbI <sub>3</sub>	1.494	1.500	0.452	Yes
53	FA <sub>0.792</sub> MA <sub>0.208</sub> PbI <sub>3</sub>	1.491	1.500	0.354	No
54	FA <sub>0.783</sub> MA <sub>0.217</sub> PbI <sub>3</sub>	1.492	1.502	0.403	No
55	FA <sub>0.783</sub> MA <sub>0.217</sub> PbI <sub>3</sub>	1.502	1.512	0.518	No
56	FA <sub>0.782</sub> MA <sub>0.218</sub> PbI <sub>3</sub>	1.498	1.505	0.504	No
57	FA <sub>0.779</sub> MA <sub>0.221</sub> PbI <sub>3</sub>	1.503	1.512	-	-
58	FA <sub>0.767</sub> MA <sub>0.233</sub> PbI <sub>3</sub>	1.494	1.503	0.446	No
59	FA <sub>0.767</sub> MA <sub>0.233</sub> PbI <sub>3</sub>	1.508	1.513	0.628	No
60	FA <sub>0.767</sub> MA <sub>0.233</sub> PbI <sub>3</sub>	1.494	1.505	0.623	No
61	FA <sub>0.750</sub> MA <sub>0.250</sub> PbI <sub>3</sub>	1.494	1.508	0.480	No
62	FA <sub>0.750</sub> MA <sub>0.250</sub> PbI <sub>3</sub>	1.506	1.514	0.576	No
63	FA <sub>0.750</sub> MA <sub>0.250</sub> PbI <sub>3</sub>	1.492	1.505	0.551	No
64	FA <sub>0.738</sub> MA <sub>0.262</sub> PbI <sub>3</sub>	1.493	1.504	0.532	No
65	FA <sub>0.733</sub> MA <sub>0.267</sub> PbI <sub>3</sub>	1.487	1.505	0.531	No
66	FA <sub>0.733</sub> MA <sub>0.267</sub> PbI <sub>3</sub>	1.503	1.514	0.320	No
67	FA <sub>0.733</sub> MA <sub>0.267</sub> PbI <sub>3</sub>	1.497	1.509	0.621	No
68	FA <sub>0.733</sub> MA <sub>0.267</sub> PbI <sub>3</sub>	1.490	1.500	-	-
69	FA <sub>0.724</sub> MA <sub>0.276</sub> PbI <sub>3</sub>	1.504	1.514	-	-
70	FA <sub>0.717</sub> MA <sub>0.283</sub> PbI <sub>3</sub>	1.495	1.500	-	-
71	FA <sub>0.717</sub> MA <sub>0.283</sub> PbI <sub>3</sub>	1.503	1.512	-	-
72	FA <sub>0.712</sub> MA <sub>0.288</sub> PbI <sub>3</sub>	1.498	1.512	0.555	No

**Table S-1:** Continued from previous page.

Sample	Computed Composition	Auto $E_g$ (eV)	Expert $E_g$ (eV)	$I_c$ (px·hr)×10 <sup>5</sup>	Degradation (Ground Truth)
73	FA <sub>0.700</sub> MA <sub>0.300</sub> PbI <sub>3</sub>	1.505	1.512	0.477	No
74	FA <sub>0.700</sub> MA <sub>0.300</sub> PbI <sub>3</sub>	1.499	1.510	0.414	No
75	FA <sub>0.697</sub> MA <sub>0.303</sub> PbI <sub>3</sub>	1.501	1.510	0.433	No
76	FA <sub>0.686</sub> MA <sub>0.314</sub> PbI <sub>3</sub>	1.511	1.522	0.567	No
77	FA <sub>0.683</sub> MA <sub>0.317</sub> PbI <sub>3</sub>	1.502	1.510	0.595	-
78	FA <sub>0.683</sub> MA <sub>0.317</sub> PbI <sub>3</sub>	1.503	1.510	0.528	No
79	FA <sub>0.683</sub> MA <sub>0.317</sub> PbI <sub>3</sub>	1.514	1.525	-	No
80	FA <sub>0.677</sub> MA <sub>0.323</sub> PbI <sub>3</sub>	1.502	1.510	0.282	No
81	FA <sub>0.667</sub> MA <sub>0.333</sub> PbI <sub>3</sub>	1.516	1.528	0.498	No
82	FA <sub>0.667</sub> MA <sub>0.333</sub> PbI <sub>3</sub>	1.504	1.515	0.423	No
83	FA <sub>0.667</sub> MA <sub>0.333</sub> PbI <sub>3</sub>	1.498	1.510	0.219	No
84	FA <sub>0.650</sub> MA <sub>0.350</sub> PbI <sub>3</sub>	1.501	1.510	0.353	No
85	FA <sub>0.650</sub> MA <sub>0.350</sub> PbI <sub>3</sub>	1.502	1.510	0.383	No
86	FA <sub>0.650</sub> MA <sub>0.350</sub> PbI <sub>3</sub>	1.507	1.515	0.302	No
87	FA <sub>0.625</sub> MA <sub>0.375</sub> PbI <sub>3</sub>	1.503	1.513	0.250	No
88	FA <sub>0.624</sub> MA <sub>0.376</sub> PbI <sub>3</sub>	1.510	1.515	0.389	No
89	FA <sub>0.617</sub> MA <sub>0.383</sub> PbI <sub>3</sub>	1.509	1.520	0.335	No
90	FA <sub>0.614</sub> MA <sub>0.386</sub> PbI <sub>3</sub>	1.505	1.515	0.196	No
91	FA <sub>0.611</sub> MA <sub>0.389</sub> PbI <sub>3</sub>	1.522	1.530	0.549	No
92	FA <sub>0.600</sub> MA <sub>0.400</sub> PbI <sub>3</sub>	1.518	1.530	0.391	No
93	FA <sub>0.600</sub> MA <sub>0.400</sub> PbI <sub>3</sub>	1.509	1.520	0.255	No
94	FA <sub>0.600</sub> MA <sub>0.400</sub> PbI <sub>3</sub>	1.509	1.520	0.241	No
95	FA <sub>0.583</sub> MA <sub>0.417</sub> PbI <sub>3</sub>	1.510	1.520	0.331	No
96	FA <sub>0.583</sub> MA <sub>0.417</sub> PbI <sub>3</sub>	1.511	1.522	0.280	No
97	FA <sub>0.583</sub> MA <sub>0.417</sub> PbI <sub>3</sub>	1.518	1.530	0.344	No
98	FA <sub>0.569</sub> MA <sub>0.431</sub> PbI <sub>3</sub>	1.512	1.523	0.303	No
99	FA <sub>0.567</sub> MA <sub>0.433</sub> PbI <sub>3</sub>	1.520	1.530	0.325	No
100	FA <sub>0.567</sub> MA <sub>0.433</sub> PbI <sub>3</sub>	1.508	1.520	0.429	No
101	FA <sub>0.559</sub> MA <sub>0.441</sub> PbI <sub>3</sub>	1.501	1.510	0.433	No
102	FA <sub>0.558</sub> MA <sub>0.442</sub> PbI <sub>3</sub>	1.512	1.526	0.366	No
103	FA <sub>0.558</sub> MA <sub>0.442</sub> PbI <sub>3</sub>	1.511	1.523	0.320	No
104	FA <sub>0.550</sub> MA <sub>0.450</sub> PbI <sub>3</sub>	1.524	1.530	0.414	No
105	FA <sub>0.550</sub> MA <sub>0.450</sub> PbI <sub>3</sub>	1.503	1.510	0.270	No
106	FA <sub>0.545</sub> MA <sub>0.455</sub> PbI <sub>3</sub>	1.513	1.523	0.365	No
107	FA <sub>0.533</sub> MA <sub>0.467</sub> PbI <sub>3</sub>	1.517	1.532	0.372	No
108	FA <sub>0.533</sub> MA <sub>0.467</sub> PbI <sub>3</sub>	1.509	1.520	0.288	No
109	FA <sub>0.529</sub> MA <sub>0.471</sub> PbI <sub>3</sub>	1.515	1.526	0.252	No
110	FA <sub>0.517</sub> MA <sub>0.483</sub> PbI <sub>3</sub>	1.529	1.532	0.282	No
111	FA <sub>0.517</sub> MA <sub>0.483</sub> PbI <sub>3</sub>	1.523	1.530	0.340	No
112	FA <sub>0.517</sub> MA <sub>0.483</sub> PbI <sub>3</sub>	1.513	1.528	0.356	No
113	FA <sub>0.511</sub> MA <sub>0.489</sub> PbI <sub>3</sub>	1.528	1.532	0.286	No

**Table S-1:** Continued from previous page.

Sample	Computed Composition	Auto $E_g$ (eV)	Expert $E_g$ (eV)	$I_c$ (px·hr)×10 <sup>5</sup>	Degradation (Ground Truth)
114	FA <sub>0.504</sub> MA <sub>0.496</sub> PbI <sub>3</sub>	1.514	1.530	0.270	No
115	FA <sub>0.500</sub> MA <sub>0.500</sub> PbI <sub>3</sub>	1.500	1.535	0.254	No
116	FA <sub>0.500</sub> MA <sub>0.500</sub> PbI <sub>3</sub>	1.518	1.530	0.216	No
117	FA <sub>0.498</sub> MA <sub>0.502</sub> PbI <sub>3</sub>	1.518	1.525	0.253	No
118	FA <sub>0.483</sub> MA <sub>0.517</sub> PbI <sub>3</sub>	1.522	1.525	0.244	No
119	FA <sub>0.459</sub> MA <sub>0.541</sub> PbI <sub>3</sub>	1.524	1.530	0.210	No
120	FA <sub>0.450</sub> MA <sub>0.550</sub> PbI <sub>3</sub>	1.523	1.530	0.241	No
121	FA <sub>0.447</sub> MA <sub>0.553</sub> PbI <sub>3</sub>	1.520	1.530	0.306	No
122	FA <sub>0.445</sub> MA <sub>0.555</sub> PbI <sub>3</sub>	1.530	1.537	0.282	No
123	FA <sub>0.433</sub> MA <sub>0.567</sub> PbI <sub>3</sub>	1.523	1.530	0.331	No
124	FA <sub>0.433</sub> MA <sub>0.567</sub> PbI <sub>3</sub>	1.527	1.533	0.305	No
125	FA <sub>0.433</sub> MA <sub>0.567</sub> PbI <sub>3</sub>	1.529	1.537	0.288	No
126	FA <sub>0.417</sub> MA <sub>0.583</sub> PbI <sub>3</sub>	1.524	1.533	0.416	No
127	FA <sub>0.417</sub> MA <sub>0.583</sub> PbI <sub>3</sub>	1.525	1.530	0.262	No
128	FA <sub>0.417</sub> MA <sub>0.583</sub> PbI <sub>3</sub>	1.528	1.537	0.351	No
129	FA <sub>0.402</sub> MA <sub>0.598</sub> PbI <sub>3</sub>	1.524	1.533	0.312	No
130	FA <sub>0.400</sub> MA <sub>0.600</sub> PbI <sub>3</sub>	1.518	1.530	0.248	No
131	FA <sub>0.400</sub> MA <sub>0.600</sub> PbI <sub>3</sub>	1.521	1.530	0.287	No
132	FA <sub>0.400</sub> MA <sub>0.600</sub> PbI <sub>3</sub>	1.527	1.539	0.408	No
133	FA <sub>0.392</sub> MA <sub>0.608</sub> PbI <sub>3</sub>	1.524	1.530	0.279	No
134	FA <sub>0.391</sub> MA <sub>0.609</sub> PbI <sub>3</sub>	1.527	1.535	0.271	No
135	FA <sub>0.383</sub> MA <sub>0.617</sub> PbI <sub>3</sub>	1.531	1.538	0.347	No
136	FA <sub>0.383</sub> MA <sub>0.617</sub> PbI <sub>3</sub>	1.517	1.530	0.457	No
137	FA <sub>0.367</sub> MA <sub>0.633</sub> PbI <sub>3</sub>	1.529	1.539	0.274	No
138	FA <sub>0.367</sub> MA <sub>0.633</sub> PbI <sub>3</sub>	1.527	1.535	0.410	No
139	FA <sub>0.367</sub> MA <sub>0.633</sub> PbI <sub>3</sub>	1.530	1.540	0.278	No
140	FA <sub>0.360</sub> MA <sub>0.640</sub> PbI <sub>3</sub>	1.529	1.540	0.352	No
141	FA <sub>0.350</sub> MA <sub>0.650</sub> PbI <sub>3</sub>	1.529	1.540	0.332	No
142	FA <sub>0.350</sub> MA <sub>0.650</sub> PbI <sub>3</sub>	1.528	1.535	0.256	No
143	FA <sub>0.350</sub> MA <sub>0.650</sub> PbI <sub>3</sub>	1.531	1.540	0.347	No
144	FA <sub>0.342</sub> MA <sub>0.658</sub> PbI <sub>3</sub>	1.531	1.540	0.335	No
145	FA <sub>0.336</sub> MA <sub>0.664</sub> PbI <sub>3</sub>	1.529	1.535	0.291	No
146	FA <sub>0.333</sub> MA <sub>0.667</sub> PbI <sub>3</sub>	1.532	1.542	0.227	No
147	FA <sub>0.333</sub> MA <sub>0.667</sub> PbI <sub>3</sub>	1.532	1.542	0.369	No
148	FA <sub>0.332</sub> MA <sub>0.668</sub> PbI <sub>3</sub>	1.529	1.540	0.289	No
149	FA <sub>0.317</sub> MA <sub>0.683</sub> PbI <sub>3</sub>	1.532	1.540	0.244	No
150	FA <sub>0.304</sub> MA <sub>0.696</sub> PbI <sub>3</sub>	1.535	1.542	0.283	No
151	FA <sub>0.303</sub> MA <sub>0.697</sub> PbI <sub>3</sub>	1.531	1.542	0.281	No
152	FA <sub>0.292</sub> MA <sub>0.708</sub> PbI <sub>3</sub>	1.530	1.540	0.236	No
153	FA <sub>0.280</sub> MA <sub>0.720</sub> PbI <sub>3</sub>	1.533	1.546	0.254	No
154	FA <sub>0.278</sub> MA <sub>0.722</sub> PbI <sub>3</sub>	1.537	1.545	0.266	No

**Table S-1:** Continued from previous page.

Sample	Computed Composition	Auto $E_g$ (eV)	Expert $E_g$ (eV)	$I_c$ (px·hr)×10 <sup>5</sup>	Degradation (Ground Truth)
155	FA <sub>0.276</sub> MA <sub>0.724</sub> PbI <sub>3</sub>	1.529	1.540	0.276	No
156	FA <sub>0.267</sub> MA <sub>0.733</sub> PbI <sub>3</sub>	1.538	1.548	0.243	No
157	FA <sub>0.267</sub> MA <sub>0.733</sub> PbI <sub>3</sub>	1.532	1.548	0.312	No
158	FA <sub>0.267</sub> MA <sub>0.733</sub> PbI <sub>3</sub>	1.530	1.540	0.305	No
159	FA <sub>0.250</sub> MA <sub>0.750</sub> PbI <sub>3</sub>	1.537	1.547	0.258	No
160	FA <sub>0.250</sub> MA <sub>0.750</sub> PbI <sub>3</sub>	1.534	1.540	0.333	No
161	FA <sub>0.250</sub> MA <sub>0.750</sub> PbI <sub>3</sub>	1.538	1.547	0.354	No
162	FA <sub>0.234</sub> MA <sub>0.766</sub> PbI <sub>3</sub>	1.537	1.548	0.344	No
163	FA <sub>0.233</sub> MA <sub>0.767</sub> PbI <sub>3</sub>	1.530	1.540	0.331	No
164	FA <sub>0.233</sub> MA <sub>0.767</sub> PbI <sub>3</sub>	1.538	1.550	0.441	No
165	FA <sub>0.233</sub> MA <sub>0.767</sub> PbI <sub>3</sub>	1.525	1.533	0.312	No
166	FA <sub>0.226</sub> MA <sub>0.774</sub> PbI <sub>3</sub>	1.538	1.550	0.353	No
167	FA <sub>0.221</sub> MA <sub>0.779</sub> PbI <sub>3</sub>	1.539	1.550	0.433	No
168	FA <sub>0.217</sub> MA <sub>0.783</sub> PbI <sub>3</sub>	1.540	1.550	0.501	No
169	FA <sub>0.217</sub> MA <sub>0.783</sub> PbI <sub>3</sub>	1.524	1.535	0.457	No
170	FA <sub>0.200</sub> MA <sub>0.800</sub> PbI <sub>3</sub>	1.540	1.550	0.344	No
171	FA <sub>0.200</sub> MA <sub>0.800</sub> PbI <sub>3</sub>	1.532	1.540	0.415	No
172	FA <sub>0.200</sub> MA <sub>0.800</sub> PbI <sub>3</sub>	1.542	1.550	0.541	No
173	FA <sub>0.191</sub> MA <sub>0.809</sub> PbI <sub>3</sub>	1.539	1.550	0.361	No
174	FA <sub>0.183</sub> MA <sub>0.817</sub> PbI <sub>3</sub>	1.536	1.540	0.470	No
175	FA <sub>0.183</sub> MA <sub>0.817</sub> PbI <sub>3</sub>	1.545	1.550	0.229	No
176	FA <sub>0.183</sub> MA <sub>0.817</sub> PbI <sub>3</sub>	1.548	1.552	0.324	No
177	FA <sub>0.172</sub> MA <sub>0.828</sub> PbI <sub>3</sub>	1.539	1.552	0.503	No
178	FA <sub>0.167</sub> MA <sub>0.833</sub> PbI <sub>3</sub>	1.537	1.545	0.307	No
179	FA <sub>0.167</sub> MA <sub>0.833</sub> PbI <sub>3</sub>	1.547	1.552	0.247	No
180	FA <sub>0.166</sub> MA <sub>0.834</sub> PbI <sub>3</sub>	1.539	1.552	0.489	No
181	FA <sub>0.163</sub> MA <sub>0.837</sub> PbI <sub>3</sub>	1.537	1.545	0.374	No
182	FA <sub>0.150</sub> MA <sub>0.850</sub> PbI <sub>3</sub>	1.537	1.546	0.316	No
183	FA <sub>0.150</sub> MA <sub>0.850</sub> PbI <sub>3</sub>	1.536	1.552	0.209	No
184	FA <sub>0.133</sub> MA <sub>0.867</sub> PbI <sub>3</sub>	1.540	1.550	0.345	No
185	FA <sub>0.125</sub> MA <sub>0.875</sub> PbI <sub>3</sub>	1.544	1.552	0.261	No
186	FA <sub>0.117</sub> MA <sub>0.883</sub> PbI <sub>3</sub>	1.544	1.550	0.300	No
187	FA <sub>0.112</sub> MA <sub>0.888</sub> PbI <sub>3</sub>	1.553	1.556	0.279	No
188	FA <sub>0.111</sub> MA <sub>0.889</sub> PbI <sub>3</sub>	1.550	1.555	0.276	No
189	FA <sub>0.109</sub> MA <sub>0.891</sub> PbI <sub>3</sub>	1.545	1.550	0.383	No
190	FA <sub>0.100</sub> MA <sub>0.900</sub> PbI <sub>3</sub>	1.548	1.555	0.309	No
191	FA <sub>0.100</sub> MA <sub>0.900</sub> PbI <sub>3</sub>	1.549	1.560	0.494	No
192	FA <sub>0.100</sub> MA <sub>0.900</sub> PbI <sub>3</sub>	1.540	1.550	0.368	No
193	FA <sub>0.083</sub> MA <sub>0.917</sub> PbI <sub>3</sub>	1.541	1.550	0.468	No
194	FA <sub>0.083</sub> MA <sub>0.917</sub> PbI <sub>3</sub>	1.549	1.560	0.434	No
195	FA <sub>0.083</sub> MA <sub>0.917</sub> PbI <sub>3</sub>	1.548	1.555	0.361	No

**Table S-1:** Continued from previous page.

Sample	Computed Composition	Auto $E_g$ (eV)	Expert $E_g$ (eV)	$I_c$ (px·hr)×10 <sup>5</sup>	Degradation (Ground Truth)
196	FA <sub>0.067</sub> MA <sub>0.933</sub> PbI <sub>3</sub>	1.552	1.555	0.442	No
197	FA <sub>0.067</sub> MA <sub>0.933</sub> PbI <sub>3</sub>	1.547	1.560	0.444	No
198	FA <sub>0.067</sub> MA <sub>0.933</sub> PbI <sub>3</sub>	1.537	1.550	0.543	No
199	FA <sub>0.067</sub> MA <sub>0.933</sub> PbI <sub>3</sub>	1.551	1.558	0.516	No
200	FA <sub>0.067</sub> MA <sub>0.933</sub> PbI <sub>3</sub>	1.533	1.548	0.554	No
201	FA <sub>0.058</sub> MA <sub>0.942</sub> PbI <sub>3</sub>	1.553	1.560	0.498	No

## References

- [1] Wang, T. *et al.* Indirect to direct bandgap transition in methylammonium lead halide perovskite. *Energy Environ. Sci.* **10**, 509–515 (2017).
- [2] Targhi, F. F., Jalili, Y. S. & Kanjouri, F. Mapbi3 and fapbi3 perovskites as solar cells: Case study on structural, electrical and optical properties. *Results Phys.* **10**, 616–627 (2018).
- [3] Kubelka, P. & Munk, F. A contribution to the optics of pigments. *Z. Technol. Phys.* **12**, 593–599 (1931).
- [4] Makula, P., Pacia, M. & Macyk, W. How to correctly determine the band gap energy of modified semiconductor photocatalysts based on uv-vis spectra. *J. Phys. Chem. Lett.* **9**, 6814–6817 (2018).
- [5] Tauc, J., Grigorovici, R. & Vancu, A. Optical properties and electronic structure of amorphous germanium. *Phys. Status Solidi B* **15**, 627–637 (1966).
- [6] Stoumpos, C. C., Mao, L., Malliakas, C. D. & Kanatzidis, M. G. Structure-band gap relationships in hexagonal polytypes and low-dimensional structures of hybrid tin iodide perovskites. *Inorg. Chem.* **56**, 56–73 (2017).
- [7] Sun, S. *et al.* A data fusion approach to optimize compositional stability of halide perovskites. *Matter* **4**, 1305–1322 (2021).
- [8] Nan, Z. A. *et al.* Revealing phase evolution mechanism for stabilizing formamidinium-based lead halide perovskites by a key intermediate phase. *Chem* **7**, 2513–2526 (2021).
- [9] Wu, J., Chen, J. & Wang, H. Phase transition kinetics of mapbi3 for tetragonal-to-orthorhombic evolution. *JACS Au* **3**, 1205–1212 (2023).
- [10] Elsayed, M. R., Elseman, A. M., Abdelmageed, A. A., Hashem, H. M. & Hassen, A. Synthesis and numerical simulation of formamidinium-based perovskite solar cells: a predictable device performance at nis-egypt. *Sci. Reports* **13**, 1–16 (2023).
- [11] Wang, T. *et al.* Sustainable materials acceleration platform reveals stable and efficient wide-bandgap metal halide perovskite alloys. *Matter* **6**, 2963–2986 (2023).
- [12] Ahmadi, M., Ziatdinov, M., Zhou, Y., Lass, E. A. & Kalinin, S. V. Machine learning for high-throughput experimental exploration of metal halide perovskites. *Joule* **5**, 2797–2822 (2021).
- [13] Wang, Z. *et al.* Efficient ambient-air-stable solar cells with 2d–3d heterostructured butylammonium-caesium- formamidinium lead halide perovskites. *Nat. Energy* **2**, 1–10 (2017).

- [14] Sun, S. *et al.* Accelerated development of perovskite-inspired materials via high-throughput synthesis and machine-learning diagnosis. *Joule* **3**, 1437–1451 (2019).
- [15] Liu, A. *et al.* High-performance metal halide perovskite transistors. *Nat. Electron.* 1–13 (2023).